

# CLASSIFICATION BETWEEN PRECIPITATION AND VOLCANIC CLOUDS USING

## Poster2-48 OPERATIONAL X-BAND POLARIMETRIC RADAR PARAMETERS

Y. Kim

Research and Education Center for Natural Hazards, Kagoshima University, Korimoto, Kagoshima, Japan

M. Maki \*

Research and Education Center for Natural Hazards, Kagoshima University, Korimoto, Kagoshima, Japan

M. Iguchi

Sakurajima Volcano Research Center/DPRI, Kyoto University, Sakurajima, Kagoshima, Japan

D.I. Lee

Department of Environmental Atmospheric Sciences, Pukyong National University, Namgu, Busan, Korea

### 1. INTRODUCTION

Explosive volcanic eruptions are severe natural phenomena that produce pyroclastic materials, eruption columns, and volcanic ash clouds. During moist weather conditions, volcanic eruption products can be coated with water, resulting in wet ash and/or mixtures of ash and rain. Wet ash, which is heavier than dry ash increases the risk of towers and poles collapsing, and rain mixed with volcanic ash is a harmful natural phenomenon that threatens human life, infrastructures, economies, agriculture, etc. Optical measurements, which are made with ground-based instruments (ex, two-dimensional video disdrometer (2DVD), parsivel, etc.), cameras, and satellites, are limited in their ability to detect volcanic ash clouds and eruption columns in cloudy or precipitation conditions. Weather radar is one of the key instruments for studying and monitoring both precipitation and volcanic ash clouds, since it can observe both types of system and can provide valuable information that can discriminate between the two systems through the use of polarimetric parameters.

In this paper, our goal is to find characteristic of polarimetric parameters for volcanic ash clouds and precipitation using observed radar data, and to make a classification algorithm for discriminating two systems.

### 2. DATA AND METHOD

#### 2.1 Data

The X-band polarimetric (X-POL) radar data were collected from Tarumizu sites (TRM; 130.69°E, 31.49°N), as shown in Figure 1. The main specifications of the TRM radar are presented in Table 1. Figure 2 is the scan strategy of the TRM radar, which were repeated every 5 min, covering an area with a radius of 80-km. The TRM radar observed low-level (1.7° and 6.0°) elevation angles at 1-min intervals alternately, and other elevation angles at 5-min intervals.

The polarimetric parameters measured by TRM radar were horizontal polarization  $Z_H$ , differential reflectivity  $Z_{DR}$ , differential phase shift  $\Phi_{DP}$ , copolar correlation coefficient  $\rho_{HV}$ , Doppler velocity  $VD$ , and spectral width  $WS$ .

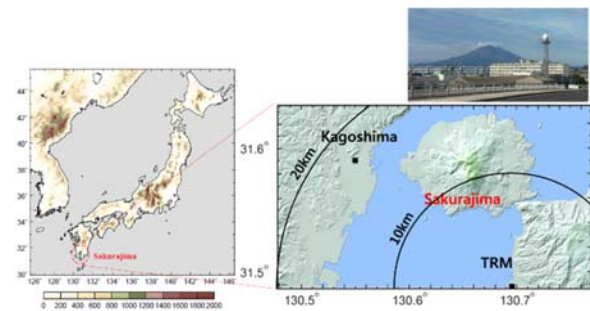


Fig. 1. Geographic map of Japan and the locations of Sakurajima and the MLIT X-band operational polarimetric radar. The photograph shows both Sakurajima volcano and the X-POL radar at the Tarumizu site. The mark (■) indicates the radar site and Kagoshima city. The circle is the observation radius of the TRM radar.

Table 1. Specifications of the TRM X-POL radar

Radar	MLIT X-band polarimetric radar
Location (Latitude/Longitude)	N 31°29'19.7" E 130°41'40.8"
Antenna size, gain, speed	2.2 mΦ, 44.7 dB(H), 45.1 dB(V), 3.5/4.0 rpm
Beam width	1.0°
Transmitter frequency	9770 MHz
PRF	1500/200 pps
Pulse width	1.0/32μs
Receiver 5 min	-109 dBm

\* Corresponding author address: M. Maki, Research and Education Center for Natural Hazards, Kagoshima Univ. Korimoto 1-21-40, Kagoshima 890-0065, Japan; e-mail: [maki@gm.kagoshima-u.ac.jp](mailto:maki@gm.kagoshima-u.ac.jp)

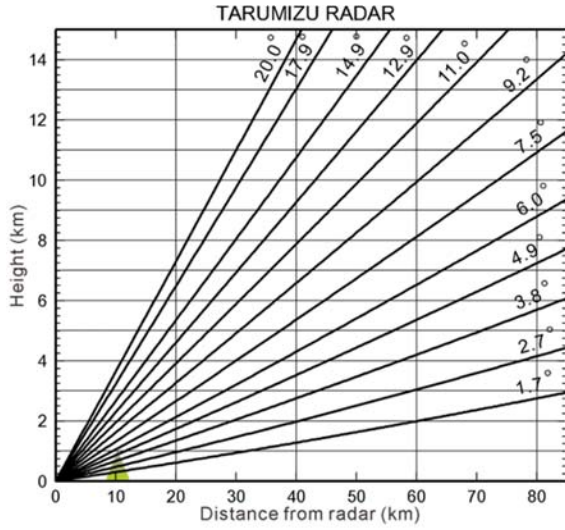


Fig. 2. Scan strategy of the X-POL operational radar. The green triangle indicates Sakurajima volcano.

## 2.2 Data processing

To remove the noise including in the radar data, morphological image processing tools were applied to the polarimetric parameters (Haralick et al., 1987; Rodrigo, 2009; Goyal, 2011). We used two applications; opening and closing. The morphological opening of A by B, denoted by  $A \ominus B$ , is simply erosion of A by B followed by the dilation of the result by B:

$$A \ominus B = (A \ominus B) \oplus B \quad (1)$$

The morphological closing of A by B, denoted by  $A \bullet B$ , is a dilation followed by an erosion:

$$A \bullet B = (A \oplus B) \ominus B \quad (2)$$

The  $\Phi_{DP}$  with morphological processing calculates for  $K_{DP}$ . The  $K_{DP}$  estimation uses the method suggested by Maesaka et al. (2012). This method can mitigate  $K_{DP}$  fluctuations in weak rainfall areas, as well as suppress fake  $K_{DP}$  caused by the backscatter differential phase  $\delta$ . However, in this method, we need to be careful of the backscatter that exists in wide areas (Maesaka et al. 2012). After  $K_{DP}$  estimation,  $K_{DP}$  fluctuations still exist in weak rainfall areas and narrow ashfall areas. We corrected  $K_{DP}$  using the empirical relationship between  $Z_H$  and  $K_{DP}$  in weak rainfall areas, which is  $K_{DP} \leq 0.3$  deg/km or  $Z_H \leq 35$  dBZ (Maki et al., 2005). If the estimated  $K_{DP}$  is larger than the empirical  $K_{DP}$ , we removed the estimated  $K_{DP}$ . Empirical  $K_{DP}$  is calculated with an empirical relationship, based on  $Z_H$  under scattering constraints, which is defined as:

$$ZK_{DP} = \alpha Z_H^\beta + sgm \quad (3)$$

where,  $ZK_{DP}$  is the empirical  $K_{DP}$  and  $sgm$  is the standard deviation of  $ZK_{DP}$  that depends on  $ZK_{DP}$ .

The corrected  $K_{DP}$  is used for attenuation corrections of  $Z_H$  and  $Z_{DR}$ . Due to scatter and

absorption by raindrops, the attenuation of signals results in fading of the  $Z_H$  and  $Z_{DR}$ . The attenuation correction of  $Z_H$  and  $Z_{DR}$  can be accomplished using  $A_h$  and  $A_{dp}$ , which are determined as a function of range. With an empirical relationship based on  $K_{DP}$ ,  $A_h$  and  $A_{dp}$  are calculated by equations (4) and (5), respectively.

$$A_h = \alpha K_{DP}^\beta \quad (4)$$

$$A_{dp} = \gamma A_h^\rho \quad (5)$$

Due to variations in raindrop shape, the coefficient  $\alpha$  varies from 0.22 to 0.323, exponent  $\beta$  varies from 1.0 to 1.12, coefficient  $\gamma$  varies from 0.114 to 0.131, and exponent  $\rho$  varies from 1.144 to 1.2. In this paper, the coefficient values are determined as mean values (Table 2). The  $Z_H$  and  $Z_{DR}$  biases of the TRM radar were estimated from the relationship between observed  $Z_H$  and  $Z_{DR}$  from radar and derived  $Z_H$  and  $Z_{DR}$  from 2DVD data, respectively.

Table 2. Relations between the  $A_h$  and  $K_{DP}$ , and  $A_{dp}$  and  $A_h$ .

Reference	$A_h = \alpha K_{DP}^\beta$		$A_{dp} = \gamma A_h^\rho$	
	$\alpha$	$\beta$	$\gamma$	$\rho$
Andsager et al. (1999)	0.293	1.101	0.128	1.156
Keenan et al. (2001)	0.315	1.120	0.114	1.144
Shi et al. (2017)	0.323	1.05	0.131	1.2
Bringi et al. (1990)	0.247	1.0	-	-
Matrosov et al. (2002)	0.22	1.0	-	-
Jameson et al. (1992)	0.233	1.0	-	-
Anagnostou et al. (2004)	0.23	1.0	-	-
Mean	0.266	1.09	0.124	1.167

The values of  $\rho_{HV}$  were corrected using signal-to-noise ratio (SNR), as described in the appendix of Shusse et al. (2009). To avoid noisy data, data that was less than 5% of the relationship  $Z_H$ - $\rho_{HV}$  were excluded from the analysis.

## 2.3 Method

Determination of the membership functions (MBF) is an important part of the fuzzy-logic-based hydrometeor classification method. In this study, the beta function  $\beta$  used by Liu et al. (2000) is employed for the MBF:

$$\beta(x, a, b, m) = \frac{1}{1 + \left[ \frac{(x-m)^2}{a} \right]^b} \quad (6)$$

where  $x$  is the input variable,  $a$  is the half-value width,  $b$  is the beta function slope, and  $m$  is the midpoint.

## 3. RESULTS

### 3.1 Overview of analyses cases

To find the distinguishable features between volcanic ash clouds and precipitation, we analyzed 12 volcanic ash cloud events (each located at heights of over 3,000 m) and 46 rain events (included convective precipitations, seasonal rain fronts, typhoons, etc.),

which occurred during the period from June to November, 2013.

### 3.2 Characteristics of polarimetric radar parameters for volcanic ash clouds and precipitation

Figure 3 to 6 show the probability density function (PDF) of polarimetric radar parameters  $Z_H$ ,  $Z_{DR}$ ,  $K_{DP}$ ,  $\rho_{HV}$ , respectively. The gray shaded areas in the figures represent the distributions of volcanic ash clouds, and the three lines (dotted, dashed, and solid) indicate precipitation according to the rain rate, which are from greater than or equal to 1 mm to less than 10 mm (light rain), from greater than or equal to 10 mm to less than 30 mm (moderate rain), from greater than or equal to 30 mm (heavy rain), respectively.

The  $Z_H$  and  $K_{DP}$  of light rain overlap volcanic ash clouds, but these moderate rain and heavy rain parameters can be separated from volcanic ash clouds. However, the range of  $Z_{DR}$  of volcanic ash clouds overlaps all types of rain except heavy rain larger than 3 dB. The range of  $\rho_{HV}$  of all types of rain is greater than 0.8, but volcanic ash clouds are less than 0.8. This can help to discriminate between volcanic ash clouds and the three types of rain.

### 3.3 MBF for classification algorithm

The analyzed characteristics of the polarimetric radar parameters are used to make the MBF for each parameter. The half-width  $a$  is calculated by maximum and minimum. However, due to these values being discontinuous, we excluded minimum values smaller than 0.5% and maximum values larger than 99.5%. Beta function slope  $b$  refers to Kouketsu et al. (2015).

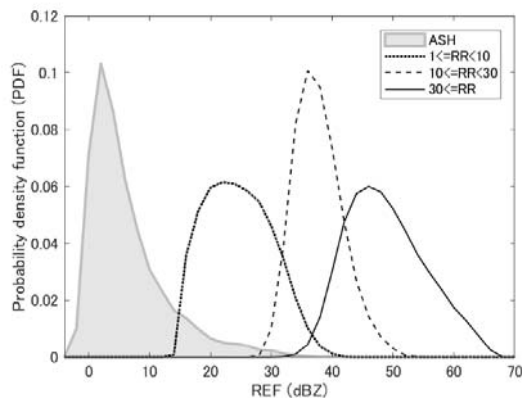


Fig. 3. Distribution of  $Z_H$  for volcanic ash clouds and precipitation according to rain rate. The gray shaded area indicates volcanic ash clouds, and the dotted, dashed, and solid lines show precipitation, which are  $1 \text{ mm} \leq \text{rain rate (RR)} < 10 \text{ mm}$ ,  $10 \text{ mm} \leq \text{RR} < 30 \text{ mm}$ ,  $30 \text{ mm} \leq \text{RR}$ , respectively.

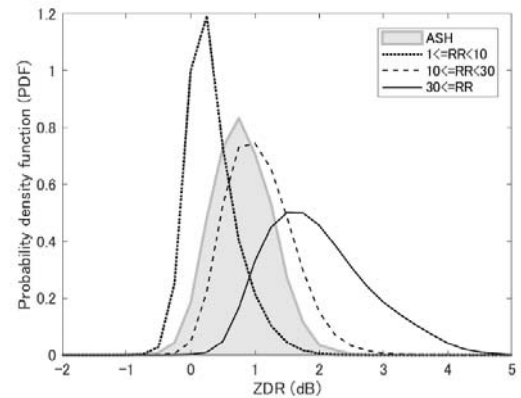


Fig. 4. Same as Fig. 3, but for  $Z_{DR}$ .

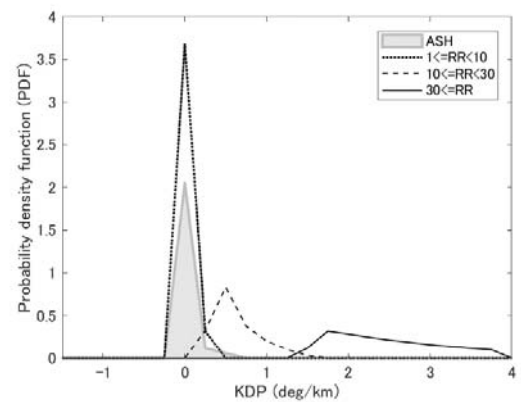


Fig. 5. Same as Fig. 3, but for  $K_{DP}$ .

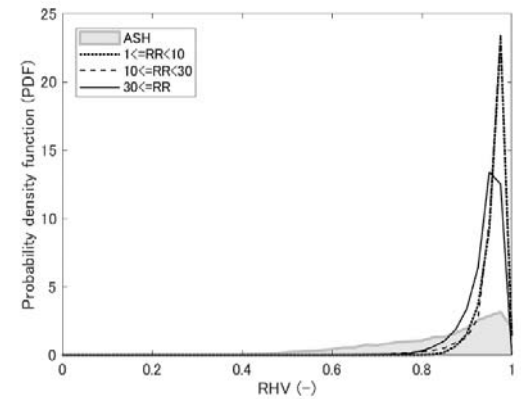


Fig. 6. Same as Fig. 3, but for  $\rho_{HV}$ .

### 3.4 Application of classification algorithm

We applied the classification algorithm for events of volcanic ash clouds and rain. Figure 7 shows volcanic ash clouds alone in the plan position indicator (PPI) at  $6^\circ$  elevation of (a)  $Z_H$ , (b)  $Z_{DR}$ , (c)  $K_{DP}$ , (d)  $\rho_{HV}$ , and (e) the result of the classification algorithm. Fig. 7e indicates that most areas are recognized to be dry ash. Figure 8 shows convective precipitations alone. Fig. 8e indicates that most areas are recognized to be rain. Heavy rain areas are especially well distinguished. Figure 9 shows the case of volcanic ash clouds under

moist conditions. The two system exists separately, which in the left cell indicates a weak rain system and the right cell indicates volcanic ash clouds. The classification algorithm cannot distinguish between the two systems (Fig. 9e). When the wind direction in Showa crater are considered, we can discriminate between the two systems (Fig. 9f).

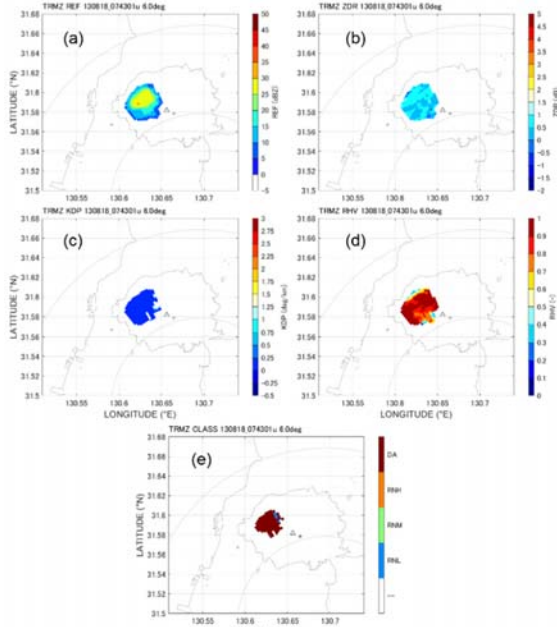


Fig. 7. The (a)  $Z_H$ , (b)  $Z_{DR}$ , (c)  $K_{DP}$ , (d)  $R_{HV}$  and (e) results of the classification algorithm in PPI at  $6^\circ$  elevation at 0743 UTC 18 Aug 2013. The triangle indicates Sakurajima and the pulse mark is the Showa crater.

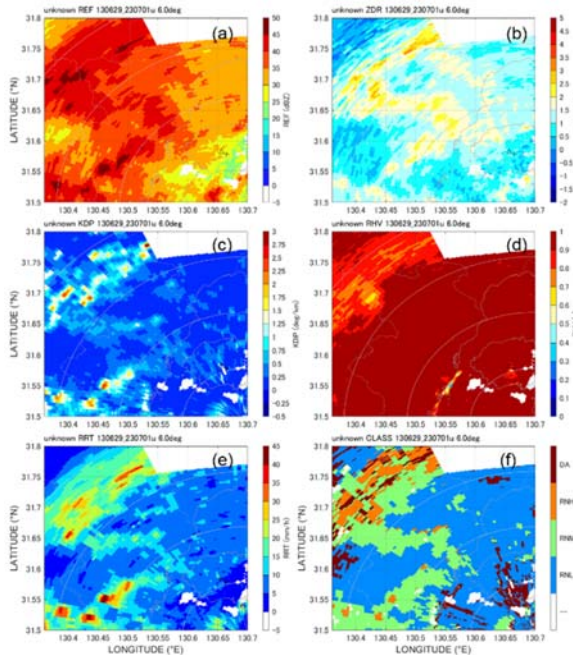


Fig. 8. Same as Fig. 7, but for (e) rain rate, and (f) the result of the classification algorithm at 2307 UTC 29 Jun 2013.

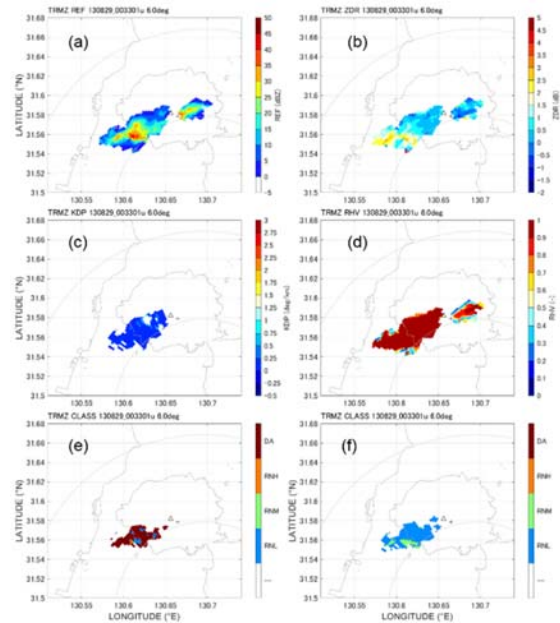


Fig. 9. Same as Fig. 7, but for (e) the result of the classification algorithm, and (f) the result of the classification algorithm with wind direction at 0033 UTC 29 Aug 2013.

#### 4. SUMMARY AND CONCLUSIONS

The characteristics of the polarimetric radar parameters of precipitation and volcanic eruption clouds were studied to make a membership function for volcanic ash clouds and rain, and to make a classification algorithm. The designed algorithm can discriminate between three conditions, which exist separately in both convective precipitations and volcanic eruption columns; convective precipitations alone, volcanic eruption columns alone, and volcanic ash clouds alone. So far, the algorithm cannot discriminate between two further conditions; when both non-convective precipitation and volcanic ash cloud exist separately, and non-convective precipitation alone (Table 3). The results of this study could help to develop and improve an algorithm that is applicable to quantitative short-term forecasting for precipitation/volcanic ash clouds (QPF/QAF) and to enhance quantitative estimation of precipitation/volcanic ash clouds (QPE/QAE). In addition, this study can also be useful in the creation of hazard maps to protect human life against harmful natural hazard phenomena, such as rain mixed with volcanic ash.

Table 3. The results of the classification algorithm.

	Eruption column	Ash cloud	No ash
Convective precipitation	$\Delta$	$\circ$	$\circ$
Non-convective precipitation	unknown	x	x
No rain	$\circ$	$\circ$	$\circ$

## ACKNOWLEDGEMENTS

This work was partially supported by MEXT “Integrated Program for Next Generation Volcano Research and Human Resource Development” and partially supported by JSPS KAKENHI Grant Number JP16H03145. The MLIT X-band polarimetric radar data used in the present study were archived and provided under the framework of the Data Integration and Analysis System (DIAS) funded by Ministry of Education, Culture, Sports, Science and Technology (MEXT).

## REFERENCES

- Anagnostou, E. N., M. N. Anagnostou, W. F. Krajewski, A. Kruger, and B. J. Miriovsky, 2004: High-resolution rainfall estimation from X-band polarimetric radar measurements. *J. Hydrometeor.*, **5**, 110-128.
- Andsager, K., K. V. Beard, and N. F. Laird, 1999: Laboratory measurements of axis ratios for large raindrops. *J. Atmos. Sci.*, **56**, 2673-2683.
- Bringi, V. N., V. Chandrasekar, N. Balakrishnan, and D. S. Zrnich, 1990: An examination of propagation effects on radar measurements at microwave frequencies. *J. Atmos. Oceanic Technol.*, **7**, 829-840.
- Goyal, M., 2011: Morphological image processing. *IJCST*, **2**(4).
- Haralick, R. M., S. R. Sternberg, X. Zhuang, 1987: Image analysis using mathematical morphology. *IEEE Trans. Pattern Anal. Machine Intell.* PAMI-**9**, 532-550.
- Jameson A. R., 1992: The effect of temperature on attenuation-correction schemes in rain using polarization propagation differential phase shift. *J. Appl. Meteor.*, **31**, 1106-1118.
- Keenan, T. D., L. D. Carey, D. S. Zrnich, and P. T. May, 2001: Sensitivity of 5-cm wavelength polarimetric radar variables to raindrop axial ratio and drop size distribution. *J. Appl. Meteor.*, **40**, 526-545.
- Kouketsu, T., and Coauthors, 2015: A hydrometeor classification method for X-band polarimetric radar: Construction and validation focusing on solid hydrometeors under moist environments. *J. Atmos. Oceanic Technol.*, **32**, 2052-2074.
- Liu, H., and V. Chandrasekar, 2000: Classification of hydrometeors based on polarimetric radar measurements: Development of fuzzy logic and neuro-fuzzy systems, and in situ verification. *J. Atmos. Oceanic Technol.*, **17**, 140-164.
- Maesaka, T., K. Iwanami, and M. Maki, 2012: Non-negative KDP estimation by monotone increasing  $\theta$ DP assumption below melting layer. *In Extended Abstracts, Seventh European Conf. On Radar in Meteorology and Hydrology*.
- Maki, M., S. G. Park, and V. N. Bringi, 2005: Effect of natural variations in rain drop size distributions on rain rate estimators of 3 cm wavelength polarimetric radar. *J. Meteor. Soc. Japan. Ser. II.*, **83**(5), 871-893.
- Matrosov, S. Y., K. A. Clark, B. E. Martner, and A. Tokay, 2002: X-band polarimetric radar measurements of rainfall. *J. Appl. Meteor.*, **41**, 941-952.
- Rodrigo, R., 2009: Morphological image processing. *Univ. Moratuwa, Moratuwa, Sri Lanka, Tech. Rep.*
- Shi, Z., H. Chen, V. Chandrasekar, and J. He, 2017: Deployment and performance of an X-band dual-polarization radar during the Southern China Monsoon Rainfall Experiment. *Atmos.*, **9**(1), 4.
- Shusse, Y., K. Nakagawa, N. Takahashi, S. Satoh, and T. Iguchi, 2009: Characteristics of polarimetric radar variables in three types of rainfalls in a Baiu front event over the East China Sea. *J. Meteor. Soc. Japan*, **87**, 865-875.